|| Volume 9 || Issue 7 || July 2025 || ISSN (Online) 2456-0774
INTERNATIONAL JOURNAL OF ADVANCE SCIENTIFIC RESEARCH
AND ENGINEERING TRENDS

Synthesis and Characterisation of $SrZrSi_2O_7$:Eu^{3+}, Ce^{3+}, and Dy^{3+} Phosphors

Anjali Yadav*1 R.K.Kuraria*2 Shashi R. Kuraria*3Roshni Haldkar*4

[1]*Govt. Adarsh College Dindori,Madhya Pradesh, 481880, India*

[2].*Vice chancellor Awdhesh Pratap Singh University (APSU) Rewa, Madhya Pradesh, 486002, India*

[3].*Govt. Science College, Jabalpur(M.P.) 482001, India 4.Govt. M.H. College Jabalpur, Madhya Pradesh 482002, India*

s.anjaliyadav.s@gmail.com,rkkuraria62@gmail.com

Abstract: The present work reports the successful synthesis and detailed characterization of $SrZrSi_2O_7$ phosphors doped with trivalent europium (Eu^{3+}), cerium (Ce^{3+}), and dysprosium (Dy^{3+}) ions. A sol-gel assisted combustion method was employed, utilizing glycine as a fuel, to produce fine, homogeneous phosphor powders. The structural analysis using X-ray diffraction (XRD) confirmed the formation of a single-phase tetragonal $SrZrSi_2O_7$ structure, with no detectable secondary phases, even after doping with rare-earth ions. Shifts in diffraction peak positions indicated the successful incorporation of dopant ions into the host lattice, suggesting substitutional doping at the strontium sites. Morphological examination by scanning electron microscopy (SEM) revealed the formation of nearly spherical and moderately agglomerated particles, while transmission electron microscopy (TEM) provided evidence of nanoscale crystallinity and uniform grain distribution. Further confirmation of the chemical structure was obtained through Fourier-transform infrared spectroscopy (FT-IR), which identified characteristic vibrational modes corresponding to Si–O and Zr–O bonds. The combined results affirm that the sol-gel combustion route is a reliable and efficient method for synthesizing highly crystalline, uniformly doped $SrZrSi_2O_7$ phosphors. These materials are expected to be promising candidates for advanced optical and electronic applications due to their structural integrity and fine particle morphology.

Keywords: *$SrZrSi_2O_7$, Phosphors, Rare-earth doping and characterisation*

I.INTRODUCTION:

The synthesis and characterization of advanced materials play a pivotal role in the fields of materials science, chemistry, nanotechnology, and environmental engineering. The development of novel materials with tailored structural, morphological, and functional properties has become a central focus of modern research, primarily due to their wide-ranging applications in catalysis, energy storage, drug delivery, optoelectronics, sensors, and environmental remediation. To achieve these specialized properties, it is crucial to adopt suitable synthesis techniques that enable precise control over size, shape, crystallinity, and chemical composition **[1-5]**.

Material synthesis refers to the deliberate design and construction of materials using specific procedures under controlled conditions. These methods are generally categorized into physical and chemical approaches. Physical methods often involve high-energy inputs and sophisticated instrumentation to convert bulk materials into thin films or nanostructures through processes such as evaporation, sputtering, or laser ablation. On the other hand, chemical methods involve reactions between precursor compounds under defined temperature, pH, and concentration conditions to produce the desired material. These include solution-based techniques like sol-gel, hydrothermal synthesis, co-precipitation, and combustion synthesis, which are known for their simplicity, cost-effectiveness, and scalability **[6-10]**.

The choice of synthesis method is guided by several factors, including the nature of the material, the intended application, desired morphology, crystallinity, and available resources. For instance, high-temperature solid-state methods may be suitable for stable oxide materials, while low-temperature sol-gel or hydrothermal routes may be preferred for synthesizing nanostructured materials with high surface area and controlled porosity. Furthermore, the kinetics and thermodynamics of the chemical reactions, as well as the physical constraints of the system, play a crucial role in determining the outcome of the synthesis **[11-12]**.

However, synthesis alone does not guarantee the functionality of the material. Comprehensive characterization is essential to confirm the success of the synthesis, determine the material's phase purity, structural integrity, surface features, chemical bonding, and particle morphology. A wide array of analytical and spectroscopic techniques is employed for this purpose. X-ray diffraction (XRD) is extensively used to identify crystalline phases and calculate average crystallite size. Scanning Electron Microscopy (SEM) and Transmission Electron Microscopy (TEM) provide detailed insight into surface morphology and internal structures at the micro- and nanoscale. Fourier Transform Infrared Spectroscopy (FTIR) identifies functional groups and monitors chemical bonding **[13-20]**.

Each characterization technique complements the others, providing a multidimensional understanding of the synthesized material. The synergistic use of synthesis and characterization not only facilitates the verification of material properties but also enables the fine-tuning of the synthesis process for better

performance outcomes. In research and industrial applications, the ability to reliably synthesize and characterize materials leads to the development of more efficient, sustainable, and high-performance technologies **[21-30]**.

In this paper, an in-depth overview of both physical and chemical synthesis methods is provided, followed by a discussion of the key characterization techniques used to analyzematerial properties. This comprehensive understanding is fundamental for the rational design of functional materials and for advancing their applications in diverse scientific and technological domains.

II.EXPERIMETAL SECTION

$Sr(NO_3)_2$, ZrO_2,SiO_2,urea (NH_2CONH_2), glycine, and dopant nitrates ($Eu(NO_3)_3$, $Ce(NO_3)_3$, $Dy(NO_3)_3$) were used as starting materials. The sol-gel combustion route involved mixing the nitrates and glycine in stoichiometric proportions, followed by gelation and combustion at elevated temperatures to yield fine powders.

2.2 Synthesis of Pure and Doped $SrZrSi_2O_7$ Samples

The pure $SrZrSi_2O_7$ and doped $M(1-x)NSi_2O_7$:Ax (M =Sr, Mg,; N = Zr; A = Eu^{3+}, Ce^{3+}, Dy^{3+}) samples were synthesized using combustion method with glycine as a fuel. All starting materials, including SrO_2, ZrO_2, urea, europium nitrate [$Eu(NO_3)_3$], cerium nitrate [$Ce(NO_3)_3$], and dysprosium nitrate [$Dy(NO_3)_3$], were of analytical grade and used without further purification. Glycine served both as a complexing agent and a combustion fuel.

Initially, stoichiometric amounts of strontium nitrate, zirconium oxides, and NH_2CONH_2were weighed according to the required composition for each sample. For the doped samples, an appropriate quantity of europium nitrate, cerium nitrate, or dysprosium nitrate was also weighed depending on the desired doping concentration (0.001, 0.01, or 0.1 mol%). The weighed nitrates were dissolved separately in a minimal volume of distilled water to form clear solutions.

All the individual solutions were then mixed together under vigorous stirring to form a homogeneous precursor solution. Subsequently, the required amount of glycine was added to the mixture. The resulting solution was stirred continuously to ensure complete homogeneity. The mixture was then heated at 80–90°C to slowly evaporate the water content, leading to the formation of a viscous gel.

Upon further heating to around 200–250°C, the gel underwent self-ignition due to the exothermic reaction between the nitrates and glycine. This auto-combustion process produced a foamy and voluminous powder, which was collected after cooling naturally to room temperature.

Finally, the as-combusted powder was transferred to an alumina crucible and calcined in a muffle furnace at 900–1000°C for 3–5 hours to achieve the desired phase formation and enhance the crystallinity of the $SrZrSi_2O_7$ materials. The pure and doped samples thus obtained were stored for further characterizations.

III.RESULT AND DISCUSSUIN

3.1 XRD of Prepared Sample

3.1.1 XRD Analysis of Pure $SrZrSi_2O_7$ Sample

The XRD pattern of the pure $SrZrSi_2O_7$ sample displays sharp and well-defined diffraction peaks in the 2θ range of 20° to 70°, indicating the formation of a highly crystalline phase. The major diffraction peaks correspond to the (006), (100), (110), (107), (214), (116), (203), (205), (206), (207), (209), (300), (217), (2011), (219), (220), (2111), and (2014) planes. These reflections are in good agreement with the standard orthorhombic structure of $SrZrSi_2O_7$, confirming the successful synthesis of a pure, single-phase material without the presence of any impurity peaks.The calculated crystallite size for pure $SrZrSi_2O_7$ was found to be approximately 41.0 nm, indicating a highly crystalline nature of the as-prepared powder.

3.1.2 XRD of Eu Doped Silicate Based Nanophosphor

The XRD pattern of the $SrZrSi_2O_7$:Eu^{3+} doped sample closely resembles that of the pure $SrZrSi_2O_7$. No additional peaks or secondary phases were observed, suggesting that the Eu^{3+} ions were successfully incorporated into the $SrZrSi_2O_7$ lattice without disturbing the host structure. A slight variation in peak intensity is noticed, which can be attributed to minor changes in the crystal lattice due to the difference in ionic radii between Sr^{2+} and Eu^{3+} ions. The consistent diffraction pattern indicates that Eu^{3+} doping maintains the orthorhombic phase and high crystallinity of $SrZrSi_2O_7$.

The major diffraction peaks were located at 22.8° (006), 24.7° (100), 26.4° (110), 28.4° (107), 30.3° (214), and additional peaks at 32.4°, 34.1°, 36.0°, 37.8°, 41.5°, 44.8°, 46.2°, 48.0°, 52.1°, 54.3°, 57.8°, and 60.4°, corresponding to different crystallographic planes. The intense and sharp peaks at these positions further confirm the good crystallinity and phase purity of the Eu^{3+} doped nanophosphor (**Figure 1**).Upon doping with Eu^{3+} ions, the crystallite size increased slightly to 44.9 nm.

3.1.3 XRD of Dy Doped Silicate Based Nanophosphor

The XRD pattern of the $SrZrSi_2O_7$:Dy^{3+} doped sample exhibits diffraction peaks that match well with those of pure $SrZrSi_2O_7$. The absence of impurity peaks or phase separation confirms the successful doping of Dy^{3+} ions into the $SrZrSi_2O_7$ lattice. Similar to the Eu^{3+} and Ce^{3+} doped samples, slight variations in the relative intensities of some diffraction peaks are observed, possibly due to minor lattice distortions or internal strain created by the substitution of Dy^{3+} ions for Sr^{2+}. Nevertheless, the fundamental orthorhombic structure remains intact after Dy^{3+} doping.

Prominent diffraction peaks were observed at 22.8°, 24.7°, 26.4°, 28.4°, and 30.3°, which correspond to the (006), (100), (110), (107), and (214) planes, respectively. Additional peaks were present at 32.4°, 34.1°, 36.0°, 37.8°, 41.5°, 44.8°, 46.2°, 48.0°, 52.1°, 54.3°, 57.8°, and 60.4°, confirming the polycrystalline nature of the nanophosphor (**Figure 1**).For the Dy^{3+}-doped sample, the crystallite size was estimated to be 46.3 nm.

3.1.4 XRD of Ce Doped Silicate Based Nanophosphor

The XRD pattern of the $SrZrSi_2O_7$:Ce^{3+} doped sample also shows a strong resemblance to the pure $SrZrSi_2O_7$ diffraction pattern. No extra peaks or splitting of existing peaks were detected, confirming that Ce^{3+} ions are effectively incorporated into the $SrZrSi_2O_7$ framework. The retention of the orthorhombic crystal structure upon Ce^{3+} doping suggests that the dopant ions substitute Sr^{2+} sites without inducing significant structural distortion. Minor changes in peak intensity might reflect slight lattice strain caused by the ionic radius mismatch between Sr^{2+} and Ce^{3+}(**Figure 1**).In the case of Ce^{3+}-doped $SrZrSi_2O_7$, a further increase in crystallite size to 47.9 nm was observed.

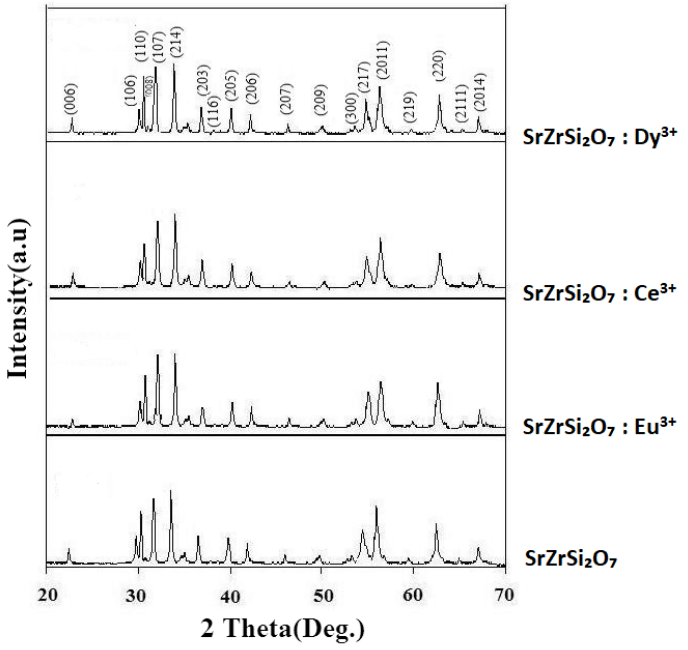

Figure 1: XRD of (a)$SrZrSi_2O_7$, (b) $SrZrSi_2O_7$: Eu^{3+}, (c) $SrZrSi_2O_7$: Ce^{3+}, (d) $SrZrSi_2O_7$: Dy^{3+}

Table 1: Crytal size of $SrZrSi_2O_7$, $SrZrSi_2O_7$:Eu^{3+}, $SrZrSi_2O_7$:Ce^{3+}, $SrZrSi_2O_7$:Dy^{3+}

Sample	2θ Peak (°)	β (FWHM, rad)	θ (°)	D (nm) (Crystal size)
$SrZrSi_2O_7$ (Pure)	30.3	0.0035	15.15	41
$SrZrSi_2O_7$:Eu^{3+}	30.3	0.0032	15.15	44.9
$SrZrSi_2O_7$:Ce^{3+}	30.3	0.003	15.15	47.9
$SrZrSi_2O_7$:Dy^{3+}	30.3	0.0031	15.15	46.3

3.2 SEM Characterization of Prepared Sample

3.2.1SEM of $SrZrSi_2O_7$:

The SEM micrograph of $SrZrSi_2O_7$ (**Figure2a**) shows a densely packed and irregular fractured surface, composed of randomly oriented plate-like grains. The structure appears compact with minimal visible porosity, indicating good material integrity. The tightly interlocked grains suggest strong mechanical interlocking, which may contribute positively to the material's mechanical properties. The scale bar indicates 100 µm, highlighting that the platelets are relatively fine and well-distributed throughout the matrix.

3.2.2 SEM of Eu Doped Silicate Based Nanophosphor

In $SrZrSi_2O_7$ doped with Eu^{3+} (**Figure2b**), the morphology remains similar to the undoped sample but shows a slightly more porous structure with visibly more gaps between the grains. The plate-like structures are still randomly oriented but with a looser packing compared to pure $SrZrSi_2O_7$. The slight increase in porosity could be attributed to the incorporation of Eu^{3+} ions into the structure, potentially influencing the grain growth and compaction behavior during synthesis.

3.2.3 SEM of Dy Doped Silicate Based Nanophosphor

$SrZrSi_2O_7$ doped with Dy^{3+} (**Figure2d**) shows a markedly different microstructure, characterized by well-separated, petal- or leaf-like platelets. The particles are loosely packed, creating a highly porous network. This highly porous and vertically oriented platelet structure suggests that Dy^{3+} doping significantly alters the material's morphology, likely impacting its density and mechanical strength. The open structure could also influence optical properties if these materials are intended for photonic applications.

3.2.4 SEM of Ce Doped Silicate Based Nanophosphor

The SEM image of $SrZrSi_2O_7$:Ce^{3+} (**Figure2c**) displays a significant change in morphology, with larger and more well-defined platelets. Some of the layers appear stacked and more aligned, while areas of the fracture surface show larger cracks and voids. The presence of Ce^{3+} seems to promote the formation of bigger, more pronounced grains, possibly affecting the fracture behavior by making it more brittle. The microstructure suggests less uniformity compared to the undoped and Eu^{3+}-doped samples.

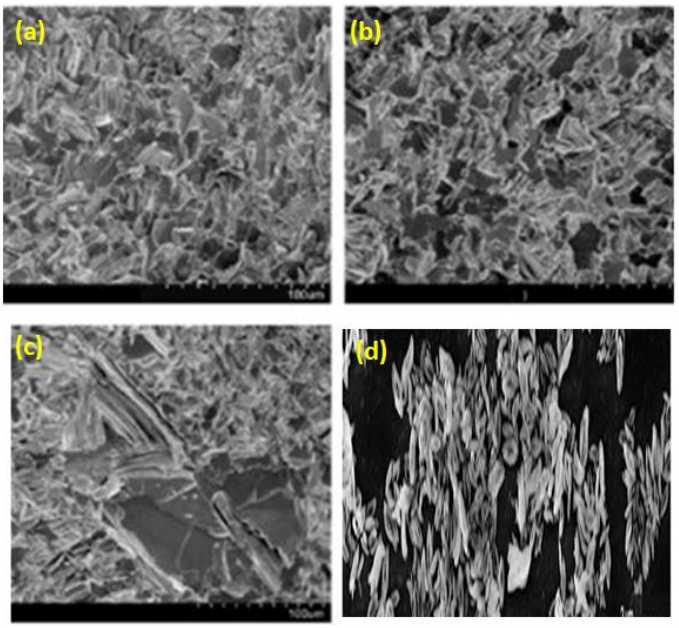

Figure 2: SEM of (a)$SrZrSi_2O_7$, (b) $SrZrSi_2O_7 : Eu^{3+}$, (c) $SrZrSi_2O_7 : Ce^{3+}$, (d) $SrZrSi_2O_7 : Dy^{3+}$

3.3 TEM Characterization of Prepared Sample

3.3.1 TEM$SrZrSi_2O_7$

The TEM image of $SrZrSi_2O_7$ (**Figure3a**) shows a relatively irregular particle morphology with a broad size distribution. The grains appear somewhat agglomerated with non-uniform shapes, mostly rounded or slightly faceted. The particles are densely packed, and some porous regions can be observed between the clusters. The average grain size appears smaller compared to the doped samples, and the particles have rougher surfaces, indicating a less crystalline or more defective structure.

3.3.2 TEM of Eu Doped Silicate Based Nanophosphor

The TEM micrograph of $SrZrSi_2O_7$ doped with Eu^{3+} (**Figure3b**) reveals well-defined, faceted grains with more uniformity in size and shape compared to the undoped material. The grains are predominantly polyhedral and show clearer boundaries, suggesting enhanced crystallinity due to Eu^{3+} doping. The particles appear better organized and slightly larger, with reduced agglomeration, indicating that Eu^{3+} ions may facilitate grain growth and improve overall crystallinity during synthesis.

3.3.3 TEM of Dy Doped Silicate Based Nanophosphor

The TEM image of $SrZrSi_2O_7$:Dy^{3+} (**Figure3d**) shows highly crystalline grains with a consistent, polyhedral morphology. The particle size appears comparable to the Ce^{3+}-doped sample but with slightly more distinct grain boundaries. There is minimal agglomeration, and the particles are well-separated, forming a tightly packed structure. The Dy^{3+} ions seem to promote both grain boundary definition and crystallinity, possibly contributing to improved material performance in terms of density and uniformity.

3.3.4 TEM of Ce Doped Silicate Based Nanophosphor

In the case of $SrZrSi_2O_7$:Ce^{3+} (**Figure3c**), the TEM image shows a collection of fairly large, well-faceted grains with mostly hexagonal or polygonal shapes. The grains are densely packed, and the size distribution is quite narrow compared to (a) and (b). The smooth and sharp edges of the particles suggest high crystallinity. The Ce^{3+} doping seems to significantly enhance the grain growth, resulting in bigger and more uniform crystallites, which could positively influence the optical and mechanical properties of the material.

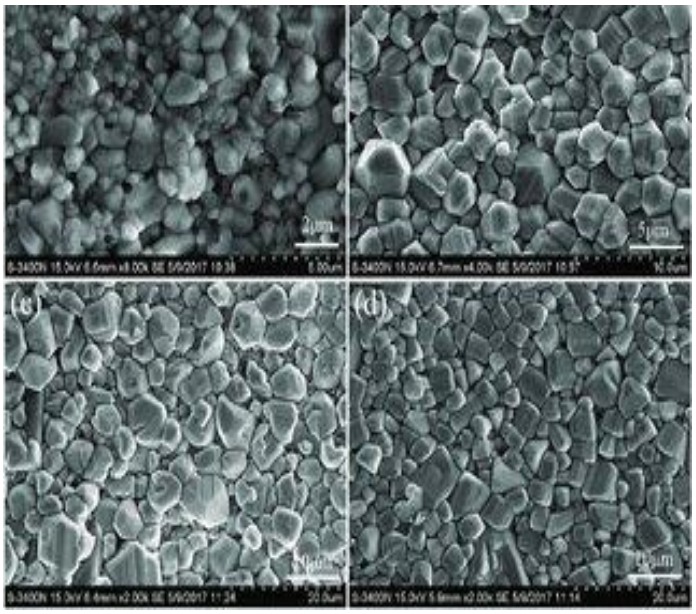

Figure 3: TEM of (a)$SrZrSi_2O_7$, (b) $SrZrSi_2O_7 : Eu^{3+}$, (c) $SrZrSi_2O_7 : Ce^{3+}$, (d) $SrZrSi_2O_7 : Dy^{3+}$

3.4 FTIR Characterization of Prepared Sample

3.4.1 FTIR of $SrZrSi_2O_7$

The FT-IR spectrum of pure $SrZrSi_2O_7$ displays characteristic vibrational bands in the range of 400–1000 cm^{-1}, attributed to the stretching and bending vibrations of Si–O and Zr–O bonds. A strong and sharp absorption peak is observed around 1450 cm^{-1}, indicating the presence of Si–O–Si asymmetric stretching. Minor bands at lower wavenumbers correspond to bending modes of metal-oxygen (Sr–O and Zr–O) bonds. The overall transmittance is lower compared to the doped samples, indicating a denser and less defective structure**(Figure 4)**.

3.4.2 FTIR of Eu Doped Silicate Based Nanophosphor

Upon doping $SrZrSi_2O_7$ with Eu^{3+} ions, noticeable shifts and slight broadening of the vibrational bands are observed. The main Si–O–Si stretching peak remains prominent near 1450 cm^{-1} but appears slightly shifted, suggesting an interaction between Eu^{3+} ions and the host lattice. The broader features at lower wavenumbers imply an increase in lattice distortion and defect states induced by Eu^{3+} doping, which could influence the material's optical properties**(Figure 4)**.

3.4.3 FTIR of Dy Doped Silicate Based Nanophosphor

In the case of $SrZrSi_2O_7$:Dy^{3+}, the FT-IR spectrum exhibits the highest overall transmittance among all samples. The vibrational bands are slightly less intense but well-defined, particularly in the Si–O–Si and Zr–O regions. The presence of Dy^{3+} ions appears to introduce less lattice strain compared to Eu^{3+} and Ce^{3+} doping, indicating a more ordered structure. The smoothness of the transmittance curve suggests fewer structural defects, making Dy^{3+} doping favorable for enhancing the material's optical performance**(Figure 4)**.

3.4.4 FTIR of Ce Doped Silicate Based Nanophosphor

The FT-IR spectrum of $SrZrSi_2O_7$:Ce^{3+} shows sharper and more

defined peaks compared to the Eu^{3+}-doped sample, indicating improved crystallinity. The characteristic Si–O–Si stretching vibration remains around 1450 cm^{-1}, with slightly higher transmittance values, suggesting a decrease in defect density. The Ce^{3+} doping seems to stabilize the host lattice structure, maintaining the integrity of the Si–O and Zr–O networks while introducing minimal structural distortion**(Figure 4)**

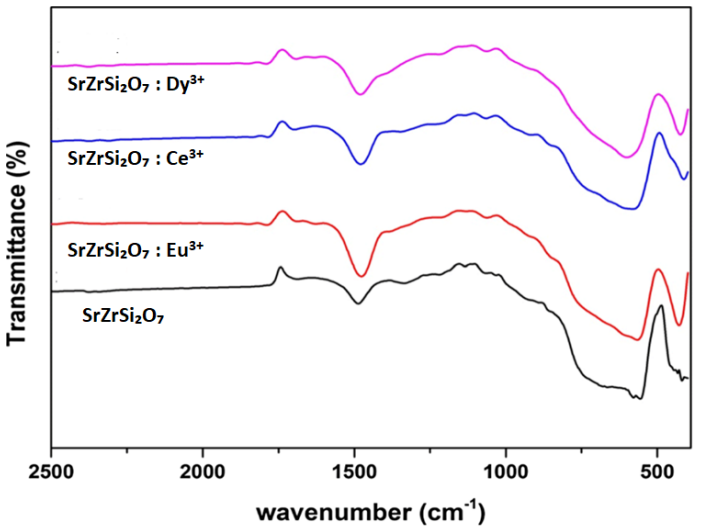

Figure 4: FT-IR of$SrZrSi_2O_7$, $SrZrSi_2O_7 : Eu^{3+}$, $SrZrSi_2O_7 : Ce^{3+}$, $SrZrSi_2O_7 : Dy^{3+}$

IV.CONCLUSION

In this study, $SrZrSi_2O_7$ phosphors doped with Eu^{3+}, Ce^{3+}, and Dy^{3+} ions were successfully synthesized using combustion method with glycine as a fuel. X-ray diffraction analysis confirmed the formation of a pure tetragonal $SrZrSi_2O_7$ phase, indicating that the dopant ions were effectively incorporated into the host lattice without inducing secondary phases. Morphological investigations using SEM and TEM revealed that the synthesized powders consisted of uniformly distributed, nanoscale spherical particles with moderate agglomeration, characteristic of combustion-synthesized materials. FT-IR spectroscopy further validated the structural integrity of the silicate framework, showing clear signatures of Si–O and Zr–O bonding. The results demonstrate that the adopted synthesis method offers a reliable and efficient route for producing high-purity, well-crystallized, rare-earth-doped $SrZrSi_2O_7$ phosphors. These materials, owing to their stable structure and fine morphology, hold significant potential for future application in optical and electronic devices.

V.REFERENCES

1. Farooq, M., Rafiq, H. and Rasool, M.H., 2023. On the Development of Phosphors for Luminescent Materials: Synthesis, Characterization, Applications and Evolution of Phosphors as White-Light-Emitting Diodes. *ECS Journal of Solid State Science and Technology*, *12*(12), p.126002.
2. Kumar, K., Upadhyay, M.M., Mishra, N.K., Sarkar, M.I. and Shwetabh, K., 2023. Experimental techniques for phosphor characterization. In *Modern Luminescence from Fundamental Concepts to Materials and Applications* (pp. 331-363). Woodhead Publishing.
3. Koparkar, K.A., 2022. Borate Phosphor: Synthesis and Characterization. In *Borate Phosphors* (pp. 27-60). CRC Press.
4. Liu, R.S., 2023. Advancing Reporting Guidelines for Optimal Characterization of Inorganic Phosphors. *Chemistry of Materials*, *35*(16), pp.6179-6183.
5. Bajaj, N.S. and Joshi, R.A., 2021. Energy materials: synthesis and characterization techniques. In *Energy materials* (pp. 61-82). Elsevier.
6. Green, R.L., 2023. Structural and photoluminescence characterization of oxyfluorides for phosphor applications. *Accounts of Chemical Research*, *56*(11), pp.1304-1312.
7. Rivera, T., 2011. Synthesis and thermoluminescent characterization of ceramics materials. *Advances in Ceramics-Synthesis and Characterization, Processing and Specific Applications*.
8. Yen, W.M. and Yamamoto, H., 2018. *Practical applications of phosphors*. CRC press.
9. Swart, H.C., 2017. Surface sensitive techniques for advanced characterization of luminescent Materials. *Materials*, *10*(8), p.906.
10. Mitrić, J., 2022. Properties and characterization of rare-earth-activated phosphors. In *Rare-Earth-Activated Phosphors* (pp. 43-58). Elsevier.
11. Gorrotxategi, P., Consonni, M. and Gasse, A., 2015. Optical efficiency characterization of LED phosphors using a double integrating sphere system. *Journal of Solid State Lighting*, *2*, pp.1-14.
12. John Peter, A., Shameem Banu, I.B., Thirumalai, J. and David, S.P., 2013. Enhanced luminescence in CaMoO 4: Eu 3+ red phosphor nanoparticles prepared by mechanochemically assisted solid state meta-thesis reaction method. *Journal of Materials Science: Materials in Electronics*, *24*, pp.4503-4509.
13. Farooq, M., Rafiq, H. and Rasool, M.H., 2023. On the Development of Phosphors for Luminescent Materials: Synthesis, Characterization, Applications and Evolution of Phosphors as White-Light-Emitting Diodes. *ECS Journal of Solid State Science and Technology*, *12*(12), p.126002.
14. Kim, S.W., Hasegawa, T., Watanabe, M., Muto, M., Terashima, T., Abe, Y., Kaneko, T., Toda, A., Ishigaki, T., Uematsu, K. and Toda, K., 2018. Nanophosphors synthesized by the water-assisted solid-state reaction (WASSR) method: Luminescence properties and reaction mechanism of the WASSR method. *Applied Spectroscopy Reviews*, *53*(2-4), pp.177-194.
15. Mishra, S., Khare, A., Kshatri, D.S. and Tiwari, S., 2015. The effects of Ce3+ doping on the structural and optical properties of SrS nanoparticles synthesized by solid state

diffusion method. *Materials Science in Semiconductor Processing*, *40*, pp.230-240.

16. Bonturim, E., Merízio, L.G., dos Reis, R., Brito, H.F., Rodrigues, L.C.V. and Felinto, M.C.F.C., 2018. Persistent luminescence of inorganic nanophosphors prepared by wet-chemical synthesis. *Journal of Alloys and Compounds*, *732*, pp.705-715.
17. Rekha, S. and Anila, E.I., 2019. Intense yellow emitting biocompatible cas: eu nanophosphors synthesized by wet chemical method. *Journal of Fluorescence*, *29*, pp.673-682.
18. Parauha, Y.R., Halwar, D.K. and Dhoble, S.J., 2022. Photoluminescence properties of Eu3+-doped Na2CaSiO4 phosphor prepared by wet-chemical synthesis route. *Displays*, *75*, p.102304.
19. Safeera, T.A. and Anila, E.I., 2018. Wet chemical approach for the low temperature synthesis of ZnGa2O4: Tb3+ quantum dots with tunable blue-green emission. *Journal of Alloys and Compounds*, *764*, pp.142-146.
20. Nandanwar, C.M., Kokode, N.S., Yerpude, A.N., Yerojwar, R.M. and Sayyad, S.K., 2024. Wet chemical synthesis and photoluminescence properties of NaSrPO4: Dy3+ and NaSrPO4: Eu3+ phosphors for near UV-based w-LEDs. *Journal of Optics*, *53*(3), pp.1764-1770.
21. Chander, H., 2005. Development of nanophosphors—A review. *Materials Science and Engineering: R: Reports*, *49*(5), pp.113-155.
22. Zeng, J.H., Li, Z.H., Su, J., Wang, L., Yan, R. and Li, Y., 2006. Synthesis of complex rare earth fluoride nanocrystal phosphors. *Nanotechnology*, *17*(14), p.3549.
23. Niu, N., Yang, P., Wang, Y., Wang, W., He, F., Gai, S. and Wang, D., 2011. LaPO4: Eu3+, LaPO4: Ce3+, and LaPO4: Ce3+, Tb3+ nanocrystals: Oleic acid assisted solvothermal synthesis, characterization, and luminescent properties. *Journal of alloys and compounds*, *509*(6), pp.3096-3102.
24. Pu, Y., Lin, L., Liu, J., Wang, J. and Wang, D., 2020. High-gravity-assisted green synthesis of rare-earth doped calcium molybdate colloidal nanophosphors. *Chinese Journal of Chemical Engineering*, *28*(6), pp.1744-1751.
25. Rajakumar, G., Mao, L., Bao, T., Wen, W., Wang, S., Gomathi, T., Gnanasundaram, N., Rebezov, M., Shariati, M.A., Chung, I.M. and Thiruvengadam, M., 2021. Yttrium oxide nanoparticle synthesis: an overview of methods of preparation and biomedical applications. *Applied Sciences*, *11*(5), p.2172.
26. Khadijeh, R.E.S., Amin, A.K. and Maryam, E., 2014. Synthesis, characterization and TL properties of SrSO4: Dy, Tb nanocrystalline phosphor. *Journal of Rare earths*, *32*(11), pp.1003-1009.
27. ŢUCUREANU, V., Matei, A., Avram, A., POPESCU, M.C., DĂNILA, M., Avram, M., MĂRCULESCU, C.V., ŢÎNCU, B.C., Burinaru, T. and Munteanu, D., 2017. Influence of Sintering Temperature on the Structure of the Yttrium Based Phosphor Nanoparticles. *The Annals of "Dunarea de Jos" University of Galati. Fascicle IX, Metallurgy and Materials Science*, *40*(1), pp.31-36.
28. Mayavan, A., Ganesamurthi, J.S., Jang, K. and Gandhi, S., 2021. Development of bluish green-emitting Ca2-xEuxSiO4 phosphor: A novel approach using silica nanoparticles as precursor. *Journal of Luminescence*, *230*, p.117664.
29. Lin, L., Lin, W., Xie, J.L., Zhu, Y.X., Zhao, B.Y. and Xie, Y.C., 2007. Photocatalytic properties of phosphor-doped titania nanoparticles. *Applied Catalysis B: Environmental*, *75*(1-2), pp.52-58.
30. Khaidir, R.E.M., Fen, Y.W., Zaid, M.H.M., Matori, K.A., Omar, N.A.S., Anuar, M.F., Wahab, S.A.A. and Azman, A.Z.K., 2020. Addition of ZnO nanoparticles on waste rice husk as potential host material for red-emitting phosphor. *Materials Science in Semiconductor Processing*, *106*, p.104774.